Imaging hydrological dynamics in karst unsaturated zones by time-lapse electrical resistivity tomography

Jian Zhang, Colette Sirieix, Dominique Genty, Fabien Salmon, Cecile Verdet, Sylvain Mateo, Shan Xu, Stephane Bujan, Ludovic Devaux, Marie Larcanche

Imaging hydrological dynamics in karst unsaturated zones by time-lapse electrical resistivity tomography

Jian Zhang [a, b, c]*, Colette Sirieix [a, b] *, Dominique Genty [c], Fabien Salmon [a, b], Cécile Verdet [a, b], Sylvain Mateo [a, b], Shan Xu [d], Stéphane Bujan [c], Ludovic Devaux [c], Marie Larcanché [a, b]

[a] *Université de Bordeaux, CNRS, Bordeaux INP, I2M, UMR 5295, F-33400, Talence, France*

[b] *Arts et Metiers Institute of Technology, CNRS, Bordeaux INP, INRAE Université, I2M, UMR 5295, F-33400 Talence, France*

[c] *Environnements et Paléoenvironnements Océaniques et Continentaux (EPOC), UMR CNRS, 5805, Université de Bordeaux, 33615 Pessac Cedex, France*

[d] *School of Civil Engineering and Mechanics, Yanshan University, Qinhuangdao, PR China*

* The corresponding authors: Jian Zhang and Colette Sirieix
E-mail: jian.zhang@u-bordeaux.fr and colette.sirieix@u-bordeaux.fr
Postal Address : Université de Bordeaux - I2M - UMR 5295 - Département GCE
Bâtiment A11, 351 Cours de la Libération, 33405 Talence Cedex

Abstract:

The hydrodynamics of karst terrain are highly complex due to the diverse fractures and reservoirs within limestone formations. The time delay between rainfall events and subsequent flow into reservoirs exhibits significant variability. However, these hydrological processes are not easily visualized in karst topography. Subsurface geophysics, specifically 2D time-lapse electrical resistivity tomography (ERT), provides an effective method for studying the relationships between hydrological and geophysical features. In our research, we adopted ERT in the Karst Critical Zone (KCZ) to visualize specific karstic zones, including cave galleries, water storage reservoirs, wetting fronts, soil layers, and potential preferential flow paths down to a depth of 20 meters. To capture spatial and seasonal variations in resistivity, we presented a comprehensive approach by combining sixteen inversion models obtained between February 2020 and September 2022 above the Villars Cave in SW-France—a well-known prehistoric cave. We used a multi-dimensional statistical technique called Hierarchical Agglomerative Clustering (HAC) to create a composite model that divided the synthetic ERT image into eight clusters representing different karst critical zones. The ERT image clearly visualized the cave gallery with high resistivity values that remained consistent throughout the seasons. Our analysis revealed a close seasonal relationship between water excess and resistivity variations in most infiltration zones, with time delays increasing with depth. The karst reservoirs, located at significant depths compared to other clusters, displayed sensitivity to changes in water excess but were primarily affected by fluctuations in water conductivity, particularly during summer or dry periods. These findings have significant implications for predicting rainwater infiltration pathways into caves, thereby assisting in the conservation and preservation of prehistoric caves and their cultural heritage.

Keywords: Electrical resistivity tomography; Karst reservoirs; Drip rate; Hierarchical agglomerative clustering; Infiltration

53 **Main manuscript content**

54 ## 1. Introduction

55 The main formation process of karst landscapes is the dissolution of carbonate
56 rocks, resulting in various types of pores, including compact and porous rock, joints,
57 fractures, and fluid conduits (Ford and Williams, 2007). Karst groundwater is one of
58 the most critical water resources worldwide, providing drinking water for
59 approximately a quarter of the world's population (Ford and Williams, 2007).
60 Improving our understanding of the complex hydrogeology of karst aquifers is of
61 considerable importance regarding the protection of drinking water resources (White,
62 2002). However, karst aquifers, like "black boxes", are typically characterized by
63 features of fracture-permeable network transport with geometric uncertainty, posing
64 observational challenges for aquifer characterizations (Vacher and Mylroie, 2002;
65 Hartmann and Baker, 2017).

66 The application of 2D time-lapse electrical resistivity tomography (ERT) has the
67 major advantage of being non-destructive and minimum-invasive when measuring the
68 electrical resistivity targeting the air/soil/rock-filled volumes and water-filled voids in
69 highly heterogeneous aquifers to analyze changes in groundwater characteristics
70 (Samouëlian et al., 2005; Vanderborght et al., 2005; Al Hagrey, 2007; Brunet et al.,
71 2010; Binley et al., 2015; Watlet et al., 2018). Several parameters contribute to
72 variations in ERT measurements, including subsurface composition, moisture content,
73 temperature, porosity, permeability, mineralization, instrumentation, noise, and survey
74 configuration (Telford et al., 1990). ERT monitoring is an extremely efficient method
75 for some hydro-geophysics studies (Kuras et al., 2009; Coscia et al., 2012; Revil et
76 al., 2012; Uhlemann et al., 2016; 2017), including investigations of heterogeneous
77 aquifers (Chen et al., 2018; Torrese et al., 2020; Yan et al., 2023), characterization of
78 water storage zones (Pope et al., 2023; Delgado-Gonzalez et al., 2023; Kadam et al.,
79 2023), and preferential flow studies (De-Carlo et al., 2021; Song et al., 2023).

80 More specifically, researchers have used ERT on karst landforms to identify

subsurface features, sinkholes, caves, and reservoir dynamics (Gautam et al., 2000 ; Zhou et al., 2002 ; Valois et al., 2010 ; Chalikakis et al., 2011 ; Robert et al., 2011; Carrière et al., 2013; Sirieix et al., 2014; Xu et al., 2017; Verdet et al., 2020; Leopold et al., 2021). For example, ERT measurements have been utilized to visualize resistivity variations in karst-unsaturated conduits, in order to assess the mingling of surface water and matrix water within the upper Floridan karst aquifer in the USA (Meyerhof et al., 2012). Moreover, ERT and magnetic resonance sounding (MRS) were employed to investigate the influence of porous matrices in controlling the water infiltration in apparent karst structures in southern France (Carrière et al., 2016). Regarding the link between resistivity changes and flow rate variations, Xu et al. (2017) revealed a close link between some cluster zones and measured underground flows in the Lascaux Cave, SW-France. More recently, Watlet et al. (2018) used long-term permanent electrical resistivity tomography (ERT) monitoring to investigate the complex karst vadose areas in Belgium. This study revealed the recharge processes with different hydro-dynamics, resulting in the clustering of different areas with a contrasting evolution during the different hydrological cycles (Watlet et al., 2018). Taken together, these studies have demonstrated the applicability of the ERT method to karst hydrological research.

The Villars Cave is a typical shallow cave that developed in Jurassic limestone, characterized by the presence of thin sandy clay Quaternary sediments at the surface, together with weathered limestone areas that likely alter the drip flow rate and geophysical signals, providing a specific geological site for geophysical research. Previous work in the Villars Cave has provided isotopic insight into the seasonality of infiltration (Genty et al., 2014; Zhang et al., 2020). However, important questions remain regarding karst reservoir dynamics and geometry, such as the size, number, and shape of karst unsaturated reservoirs and their dynamics (Genty et al., 2014). In this study, the 2D TL-ERT method was utilized to investigate and continuously monitor the subsurface geological features above the shallow Villars Cave over a monitoring period of 2.5 years. To gain a comprehensive understanding, the 2D ERT measurements were combined with soil borehole observations and hydrology

111 monitoring at three cave dripping sites. The purpose of the study is summarized as
112 follows: firstly, we visualize and precisely located various water reservoirs, wetting
113 fronts, soil layers, and cave galleries within the subsurface. This also include
114 documenting their seasonal variations in resistivity to shed light on the dynamic
115 behavior of these features. Secondly, the study seeks to explore the relationship
116 between resistivity measurements and hydrological changes in the seepage zone
117 above the cave galleries. By analyzing resistivity variations, we attempt to gain
118 insights into the intricate interplay between subsurface water flow and resistivity
119 distribution. Lastly, the study aims to identify preferential paths of water flow within
120 the unsaturated zone above the Villars Cave. By visualizing the flow pathway
121 patterns, we hope to reveal the complex hydrological dynamics occurring within the
122 cave's surroundings. By addressing these objectives, the visualization for water
123 infiltration pathways could be helpful in making strategies for the effective
124 conservation and management of cave paintings. In fact, water infiltration could
125 dissolve the paintings or, on the contrary, encourage the deposit of calcite veil that
126 covers the rock paintings. On the other hand, modeling the vadose zone in karst
127 hydrology presents challenges. This research has the potential to enhance our
128 understanding of its behavior and improve modeling accuracy for karst hydrology.
129 Understanding the reservoir and flux circulation is vital for potentially safeguarding
130 the site spatially, such as from pollution or water-related issues, thereby contributing
131 to cave protection. Ultimately, the research aims to improve water management
132 practices, ensure the sustainable utilization and conservation of essential water
133 resources, and evaluate and mitigate natural hazards linked to karst formations.

134 ## 2. Studied area and cave monitoring sites

135 The Villars Cave (45°26′18″N, 0°47′2″E; Figure 1A; 1B) is located in the north
136 of the Dordogne department, SW-France. The cave developed in a Middle Jurassic
137 (Bajocian and Bathonian) limestone formation (Figure 1D). A complex geological
138 network, over 10 km long, with orientation governed by tectonics (SE-NW), such as

the St. Pardoux fault, formed in the boundary between limestone and schist a few kilometers north of Villars (Supplementary Figure 1A). The hills, covered with oak and hornbeam, are about 50 m high (about 200 m NGF, Figure 1D), and are much less steep than in the surrounding Vézère valley, creating a smoother landscape (Genty, 2008; Zhang et al., 2020). The Villars Cave site, monitored since 1996, has led to the production of many paleo-climatological records from the study of its speleothems above the cave itself (Genty et al., 2003, 2006, 2010; Wainer et al., 2009; 2011; 2013). In addition to analyzing the stalagmites, several other factors have also been monitored, including cave temperature, pCO_2, hydrologic changes, and isotopic changes in order to better interpret the stable isotope signal within the cave. The overarching goals of this comprehensive monitoring effort were to provide a deeper understanding of the stable isotope signal within the cave environment and its implications for paleoclimate and hydrological processes (Genty et al., 2008; 2014; Zhang et al., 2020).

The Villars Cave is located in a maritime climate region with mild winters and warm summers (Figure 1A). During part of the monitoring period (2007-2022), the total annual precipitation (P) over the Villars Cave was 1052 mm (standard deviation: SD=124 mm) (Genty, 2008; Genty et al., 2014; Zhang et al., 2020). In contrast to local precipitation, which is more or less distributed throughout the year, there is a considerable seasonal variation in local air temperature, which leads to a significant seasonal variation in water-excess, and consequently to cave stalactite dripping (Genty et al., 2014). The surface layer above the Villars Cave consists of brown soil, which is unevenly distributed and of varying thickness. Some areas have thin layers of soil that are only 0-20 cm thick, while other areas have soil layers that are over 50 cm thick. In addition, in certain areas, tree roots can be seen penetrating through limestone fractures to reach the ceiling of the Villars Cave, which is about 10 meters below the surface (Genty, 2008).

3. Measurement and data processing

3.1 Meteorological data and drip discharge rate monitoring

From 2020 to 2022, outside meteorological air temperature and precipitation were collected from a weather station above the Villars Cave. The ETP (potential evapotranspiration) and excess water (also known as effective rainfall) data come from the nearby Meteo-France weather station (Saint-Martin de Freissengeas, 4.8 km East). The ETP of each grid point is calculated by the Penman-Monteith method.

Drip water monitoring sites were set at different levels in the Villars Cave to detect potential differences in the recharge of the karst aquifer (Figure 1D; Genty, 2008; Genty et al., 2014). Vil-#10A is located at the upper level of the cave, and the drip points Vil-#1B and Vil-#3 (100 m away from Vil-#10A) are about 5 m apart, located on the lower level of the cave (Supplementary Table 1; Figure 1D). The drip rate sensor (acoustic STALAGMATE sensor) recorded the drip rate frequency at 15-minute intervals from 10/2019 to 09/2022 from the surface of the sealed box equipped with the acoustic sensor.

3.2 Determination of depth and location of dripping stations by magnetic field angle method

The Magnetic Field Angle (MFA) method was used to determine the depth of the dripping stations in the Villars Cave (Supplementary Figure 2; Supplementary method). This method involves moving away from a reference point called Ground Zero (GZ) along a predetermined line with the help of a receiver loop. When the magnetic field is parallel with the ground surface, a null signal is obtained, and this point is used to measure the depth.

In the study, the depth of the Vil-#10A station in the upper cave gallery was calculated to be 14 meters below the surface. The depth of the Vil-#1B and Vil-#3 stations in the lower cave gallery was determined to be 36 meters below the surface (Figures 1C & 1D, Supplementary Table 1). Specifically, the Vil-#10A station is

193 located 4.3 meters away from the profile of ERT profile (Figures 1C & 1D). On the
194 other hand, the positions of Vil-#1B and Vil-#3 are stated to be approximately 100
195 meters away from the ERT profile shown in Figure 1C.

196 **3.3 ERT measurements**

197 ERT monitoring (Figure 1C) was established to characterize the temporal and
198 spatial variation of the unsaturated area above and near the Villars Cave. From
199 February 2020 to September 2022, we acquired 16 ERT profiles at a frequency of 1 to
200 2 months (Supplementary Table 2). After several field tests in February 2020, we
201 decided to use three different electrical arrays, including the pole-dipole array with
202 both forward and reverse measurements and an injection pulse duration of 500 ms,
203 and the gradient array with an injection pulse duration of 250 ms. The three electrical
204 arrays were concatenated before inversion. During the initial test survey, we verified
205 the repeatability of the measurements using the method proposed by Peter-Borie et al.
206 (2011). Measurements were made using a SYSCAL Pro resistivity meter with 72
207 stainless steel electrodes spaced 1 m apart making a 71 m long profile line (Figure
208 1C). The use of various permanent markers facilitated the precise relocation of the
209 survey lines. Each electrode's position was determined using a Leica® laser
210 theodolite. It is worth noting that from one survey to the next, the previous electrode
211 holes can still be identified. Therefore, the accuracy of these locations is within a
212 margin of less than 1 cm. In parallel, we also tested a 1.5 m electrode spacing to
213 obtain a greater investigation depth (106.5 m long). An inversion resistivity model
214 was calculated using the Res2Dinv® software, applying the L1 norm to the data and a
215 model associated with the refinement of the mesh model (Loke, 2004) to account for
216 large contrasts in resistivity. We performed seven iterations on each survey data set,
217 after which the absolute error stabilized. After seven iterations, the inversion model
218 misfit ranged from 0.83% to 1.7% for all 16 inversion models.

3.3.1 Temperature correction

The electrical resistivity measurement depends on the rock temperature, which varies with time. We thus have corrected the ERT measurements for temperature (Hayley et al., 2007; Genelle et al., 2012; Hermans et al., 2014). This correction requires the knowledge of the temperature in the rock mass at any given time (Salmon et al., 2023). The heat equation governing thermal diffusion therefore must be reconsidered in terms of temperature. However, this equation requires the rock's thermal diffusivity, which is unknown. We, therefore, adjusted the thermal diffusivity for the calculated temperature to match in situ measurements (Salmon et al., 2023). To do this, we placed three thermocouple sensors at 0.1 m, 0.5 m, and 1 m below the surface above the cave, close to the ERT profile location (about 3 m), and measured the air temperature both inside and outside the caves.

Using the estimated diffusivity, the heat equation was calculated in the rock mass to determine the temperature at each point within the massif over time. This temperature calculation is performed in conjunction with the time series data. Furthermore, a temperature correction was applied to the inversion resistivity data using a ratio model (equation (1)), which is commonly used to correct resistivity data with the corresponding reference temperature (Ma et al., 2011; Xu et al., 2015; 2017; Supplementary Figure 3):

$$\rho_c = \rho_i \times [1 + \delta \times (T_c - T_{\text{ref}})] \quad \textbf{Eq. (1)}$$

Where ρ_c stands for resistivity after temperature correction, ρ_i is interpreted as resistivity after inversion, and T_c represents temperature during the ERT survey. δ is the temperature slope compensation value, which is set at 0.025 by most geophysicists (Keller and Frischknecht, 1966; Besson et al., 2008). Consequently, we selected T_{ref} as the reference temperature of 12.55℃, which is the average annual temperature recorded in the cave during the entire monitoring year (Supplementary Figure 3).

3.3.2 Hierarchical Agglomerative Clustering (HAC)

In addition, in order to characterize the differences in resistivity between seasons, we need to interpret the variability observed in the different zones of ERT images. The researchers utilized a classical unsupervised classification method called Hierarchical Agglomerative Clustering (HAC) to analyze the data. HAC follows a bottom-up algorithm, as described by Saporta, 1990. This algorithm helps to create an ordering of blocks, resulting in a single image where distinct zones can be differentiated based on their seasonality. In the present study, the HAC method enables whose electrical resistivity changes in a similar manner over the years to be grouped together.

HAC is a commonly used technique in various contexts to identify heterogeneity, particularly in geotechnical studies. For example, Genelle et al. (2012) used HAC to identify geotechnical heterogeneity in a landfill cover. The method was also applied to a cave study, the prehistoric Lascaux Cave in SW-France, which allowed us to recognize the reliability of the method (Xu et al., 2015; 2017). Later, Lharti et al. (2023) compared the HAC and K-means methods in the Lascaux Cave, noting that the HAC method was particularly effective in identifying areas already known to be waterlogged or clayey.

The HAC classification was finalized using 16 ERT images captured between February 2020 and September 2022. These resistivity values after temperature corrected are logarithmized and standardized according to the following equation (Xu et al., 2015; 2017; Equation 2):

$$[log10(\rho_i)]_{DCR} = \frac{log\,10(\rho_i) - \mu[log10(\rho_i)]}{\sigma[log10(\rho_i)]} \qquad \textbf{Eq. (2)}$$

$[log10(\rho_i)]_{DCR}$ is the standardized center resistivity (DCR); ρ_i is the resistivity after corrected temperature; $\mu[log10(\rho_i)]$ is the average of the log10 (ρ_i) resistivity; σ $[log10\ (\rho_i)]$ is the standard deviation of the log10 (ρ_i) resistivity.

To perform HAC, the resistivity data assigned to the blocks are arranged in a matrix with the number of rows equal to the number of blocks and the number of

columns equal to the number of surveys. The results are generally summarized in a dendrogram, where the number of clusters needed to retain the $[log10(\rho_i)]_{DCR}$ resistivity measurements can be selected. We choose the Euclidean distance and the Ward linkage criterion for the HAC analysis methods, which allow clusters to be formed such that the sum of squares of pooling within clusters is minimized. Users then choose the number of clusters according to knowledge of the research sites and objectives.

4. Results

4.1. ERT measurements

The main measurement results were gathered in 16 ERT images made from February 2020 to September 2022 (Supplementary Figure 4). The ERT profile, from northeast (NE) to southwest (SW) on a 71 m-long profile, covers the Bajocian and Bathonian limestone formations (Supplementary Figure 1). Here, strong resistivity contrasts were observed, giving a broad picture of the cave galleries and karst reservoirs, which are more or less saturated.

The distribution of relative frequency based on 16 ERT measurements suggests that the resistivity data are mainly concentrated between 245 Ω·m and 9772 Ω·m. The highest values (165–178 m NGF) correspond to the caves, while the lower values (<245 Ω·m) correspond to the top soil. According to the frequency analysis of resistivity, the median resistivity of the limestone in the Villars Cave is 1521 Ω·m, which is higher than the resistivity of the nearby well-investigated geophysical site (Lascaux Cave) with a median of 556 Ω·m (Coniacian limestone) (Xu et al., 2016; Verdet et al., 2020). This difference suggests that the limestone in the Villars Cave has undergone less weathering compared to the limestone in the Lascaux Cave.

4.2 HAC method applied to ERT image classifications

We applied the HAC method using Minitab® version 19. This method relies on a correlation matrix derived from the normalized and standardized resistivity data. The resistivity similarity of blocks between different clusters decreases with time as the distance at which they merge increases. Conversely, blocks belonging to clusters are merged at very low distances, exhibiting similar resistivity behaviors (also see Method section). The statistical parameters for each cluster are summarized in Figure 2A. Here, the classification line corresponding to the greatest distance is selected to highlight the main characteristic research zones of stratigraphic structures. The dendrogram shows three distinct primary clusters (clusters A, B, and C) (Figure 2A). Clusters A, B, and C display median resistivity in all the ERT measurements ranging from 2321 Ω·m to 100054 Ω·m, 80 Ω·m to 1277 Ω·m, and 493 Ω·m to 2635 Ω·m, respectively. They may be composed of karst structural systems with completely different geological characteristics (Figure 2A).

To get as much detail as possible to highlight potential sub-regions, we decided to make more cutoffs (classification lines), grouped into eight clusters (see dashed lines in Figure 2A) as follows:

Cluster A, consisting of clusters 1, 7, and 8, shows the highest median value for electrical resistivity (Figure 2B). Block areas with the largest resistivity values were grouped together in cluster A (clusters 7 and 8, altitude: 165-178 m) (Figure 2B), with the high median values, ranging from 5001 to 8245 Ω·m and from 3471 Ω·m to 100054 Ω·m, respectively (Table 1). However, compared to clusters 7 and 8, cluster 1 with a slightly lower median value, ranging from 2321 Ω·m to 4957 Ω·m (Table 1), is distributed around clusters 7 and 8 (Figure 2B).

Cluster B, consisting of clusters 2 and 4, shows the lowest median values, ranging from 261 Ω·m to 1277 Ω·m and 80 Ω·m to 534 Ω·m, respectively, with most conductive areas distributed mainly on the soil surface and probably in weathered limestone zones (from NE to SW direction) at 50–60 m of the ERT profile (Table 1;

Figures 2 and 2B).

Cluster C, including clusters 3, 5, and 6, with median values ranging from 775 Ω·m to 1763 Ω·m, 1432 Ω·m to 2635 Ω·m, and 493 Ω·m to 1133 Ω·m, respectively (Table 1), is located in the middle zone between 177 m and 165 m NGF (clusters 3 and 5) and lower zones deeper than 165 m NGF (cluster 6) of the ERT profile (Figure 2B).

4.3 Rainfall amount, evapotranspiration, and drip rate

The daily hydroclimatic parameters of the Villars Cave are presented in Figure 5, including rainfall (R) and rainfall minus evapotranspiration (R-ETP), which is considered effective rainfall or water-excess when it is greater than 0. We observed that the change in water-excess is seasonal, with a maximum in winter and a minimum in summer-autumn. The total annual value of the water-excess was 477 mm in 2020 and 508 mm in 2021, respectively (Figure 3A). During the year 2022, R-ETP remained below 0 from May to October, indicating that potential evapotranspiration was higher than the precipitation during this period. This anomaly is attributed to an unusually dry year, as shown in Figure 3A.

To characterize the variability of cave dripping water, we monitored the drip-rate monitoring between September 2019 and September 2022 (Table 2), by using STALAGMATE drip counters under three drip stations located at different depths, as described in section 3.2. The discharges from the three drip water sites (Vil-#10A: depth 14m, Vil-#1B, and Vil-#3: depth 36 m) ranged from 0.60 to 180.67 (SD: 37.43) drips/min (Vil-#10A), 1.6 to 61.1 (SD: 15.29) drips/min (Vil-#1B), and 0 to 44.4 (SD: 6.96) drips/min (Vil-#3). We also noted that the drip rate of Vil-#10A and Vil-#3 stations' drip rate was more variable than that of Vil-#1B (Figure 3).

During the first cycle of 2019-2020, water-excess rose to be significantly above 0 from mid-September 2019 (Figure 3A). It took about 45 days for infiltration to be filled the reservoirs and reach the percolation threshold, allowing the water to move down into the cave (Figure 3A). As a result, there was an increase in the

354 dripping rate in November 2019 in stations Vil-#10A and Vil-#3, and in December in
355 station Vil-#1B (Figures 3B and 3C). Drip rates remained high until approximately
356 May 2020 with a general decrease until December 2020. During the humid period,
357 there was a systematic link between the water-excess and the drip rate variations in
358 Vil-#10A, with a time delay of several days as we depicted in Figure 3A. During the
359 2020-2021, the hydrological cycle of Vil-#10A and Vil-#3 dripping stations began to
360 increase in December 2020, lasting until approximately August 2021 (Figures 3A and
361 3B). The fact that the beginning of the cycle at the Vil-#1B dripping station occurred
362 later than Vil-#10A and Vil-#3, close to January or February, implies that there are
363 distinct pathways and reservoirs involved in the infiltration process across the
364 different sites (Figures 3A, 3B and 3C).

365 Once the percolation threshold was reached for the reservoirs to fill up with
366 water, we conducted a cross-correlation analysis of the three monitoring sites, Vil-
367 #10A, Vil-#3, and Vil-#1B, in order to quantify the time delay between water excess
368 and drip rates. The mean lag time have been determined in the interval of 5-9 days for
369 Vil-#10A station, 56-94 days for Vil-#1B station, and 4-11 days for Vil-#3 station
370 (Supplementary Figure 5).

371 These results show the following: (1) Vil-#10A and Vil-#3 have a similar
372 water-excess/dripping time delay even though they are located at different levels (14m
373 deep for Vil-#10A and 36 m deep for Vil-#3). (2) According to the time series, the Vil-
374 #3 station has a much more dampened dripping amplitude despite a similar time delay
375 with the Vil-#10A station. (3) At the dripping point of the Vil-#1B station, located in
376 the lower gallery, we observe a much longer time lag and lower mean drip rate
377 compared to Vil-#10A.

378 4.4 Recognition of soil layers and cave zones from ERT images

379 The superficial part of the ERT images shows low resistivity values
380 corresponding to clusters 2 and 4 (Figure 2B). Cluster 4 has a median value of 106
381 Ω·m, with a range between 80 Ω·m to 534 Ω·m (Table 1) at 5-13 m and 52-71 m on

382 the ERT profile (from NE to SW), characterized by a highly variable resistivity with
383 the HAC method (Figure 2B). The specific resistivity values were observed at these
384 locations on the ERT profile, as evidenced by the results of our soil drillings, which
385 can be identified by the nature of the soil (clay and organic matter) (Supplementary
386 Figure 6, Figure 2B). The soil's upper layer of consists of extremely weathered
387 limestone, with thicknesses exceeding 0.6 m, 0.75 m, and 0.45 m at the respective
388 locations of 9.5 m, 56 m, and 60.5 m (Figure 2B and Supplementary Figures 6 and 7).
389 Cluster 2 has a median resistivity value of 351 Ω·m, ranging from 261 Ω·m to
390 1277 Ω·m (Figure 2B; Table 1). It is situated on the surface, specifically between 15
391 m and 50 m on the profile line (from NE to SW), as well as in a deeper zone (altitude:
392 172 to 177 m, NGF) that can be seen between 50 m and 60 m on the ERT profile
393 (Figure 2B). We further divide cluster 2 into two distinct sub-clusters, namely clusters
394 2.1 and 2.2 (Figure 4A):
395 (1) Cluster 2.2, located in the superficial part of the ERT profile (Figure 4A),
396 shows a median electrical resistivity value of 219 Ω·m, with a range from
397 160 Ω·m to 1047 Ω·m (Figure 4B). The median resistivity value of cluster
398 2.2 is slightly higher but comparable to the median resistivity value of
399 cluster 4 (106 Ω·m, top-soil). Cluster 2.2 displays seasonal variations,
400 which are commonly linked to water excess (Figures 4A and 4B). The
401 surface in cluster 2.2 is confirmed to be the top soil that is about 0.2 m
402 thick, as observed at two locations situated at 24 m and 38 m on the ERT
403 profile (Figure 4B).
404 (2) The median resistivity of cluster 2.1 is 403 Ω·m, ranging from 304 Ω·m to
405 2029 Ω·m, which is higher than cluster 2.2 (Figure 4B). Cluster 2.1 is
406 associated with the soil layer situated below the layer of cluster 2.2, as well
407 as in the deeper section between 50 m to 60 m of the ERT profile (altitude:
408 172 m to 177 m, NGF) (Figure 4A). Cluster 2.1 exhibits the seasonal
409 fluctuations that are associated with the water excess (Figures 4A and 4B).
410 In particular, after digging the soil, the limestone areas were observed to be
411 undergone weathering (small limestone blocks mixed with sandy soil)

between depths of 0.4 m and over 0.75 m (56 m on the ERT profile in Figure 4B). Hence, it is possible that cluster 2.1 could represent a mixture of weathered limestone with sandy soils with high porosity. However, due to the limitations of the manual auger, it was not possible to excavate deeper to determine the exact boundary (>0.75 m) (Supplementary Figure 6 and 7).

Clusters 7 and 8 exhibit a consistently high median resistivity (7168 Ω·m) (Figure 2B), without showing seasonal variations over time (Figures 5A and 5H). The comparison of the location of these clusters with the cave plan map allowed us to attribute these zones to the cave galleries (Figures 1C and 2B), showing that: (1) Cluster 7 (Figure 2B) has high resistivity zones located on the ERT profile at 6-22 m (Zone A, Figure 1C) and 40-54 m (Zone B, Figure 1C). (2) Cluster 8 (Figure 2B), located at a vertical altitude of 168 m-178 m NGF, displays a high resistivity signal observed at 60-71 m (Zone C, Figure 1C), indicating the presence of an undiscovered cave gallery or a sinkhole collapse.

5. Discussion

5.1. Clustering resistivity variabilities with local water excess in the different ERT zones

According to Archie's law (Archie, 1942), if the electrical resistivity of a rock formation varies with time, it implies that the degree of saturation (S_w) or the resistivity of water (ρ_w) is changing with time, as the porosity (Φ) is assumed to be constant. Therefore, changes in the electrical resistivity of the rock over time can reflect changes in the rock's water content, responding to local water-excess (Xu et al., 2017).

As observed in Figure 5, there is a strong correlation between water-excess (blue part in Figure 5A) and resistivity over time. Resistivity decreases sharply following an increase in water excess as there is more water in the limestone. Here roughly, we observe a well-marked seasonality over time, with the resistivity in

clusters 1 to 5 increasing in summer and autumn, and decreasing in winter and spring (Figures 5B-5F). Furthermore, it is worth noting that each cluster displays a distinct range of resistivity values, despite some seasonal similarities exist between them (Figures 5B-5F).

To facilitate a point-to-point comparison of water excess and resistivity variability, we plotted them on the same graph for each cluster (Figures 6 and 7). The superficial part of the ERT images (essentially cluster 4 and cluster 2) displays obvious seasonal changes and represent a relatively quasi-synchronous response to the local water-excess (Figure 6A). We also noted a high variability in resistivity where the highest median value is 534 Ω·m, and the lowest median value is 80 Ω·m (cluster 4, Figure 6A). It is assumed that the resistivity of water (ρ_w) remained constant within the rock mass and assuming the porosity (φ) remained constant over time (Genty et al., 2001), we can estimate that the top soil water saturation (S) in cluster 4 varied approximately within the range of S_{min} to S_{max}, where S_{max} is approximately 2.6 times for S_{min}. In addition, the surface soil layers responded to the local drought periods of July 2020 and July-September 2022 (Rainfall-ETP<0), since high resistivity values were observed (Figure 6A). In more detail, we observed a minimum water-excess of 46.30 mm in June and July 2020 (Table 2 and Figure 6A). As a result, the relative frequency distribution of resistivity observed in the top-soil layer does not show some values less than 245 Ω·m compared to the other months (Supplementary Figure 8B). Similarly, from May 2022 to September 2022, the water-excess fell to 96.2 mm (Table 2 and Figure 6A). As a result, there was a shift in the frequency distribution of relative resistivity towards higher values, reaching peaks as high as 2563 Ω·m for the median value, and resistivity values below 245 Ω·m were no longer present (Supplementary Figure 8H). In detail, the resistivity of cluster 2.1 which is the deeper part of cluster 2 varies with the seasons. This means it could act as the role of a pathway between the superficial top-soil and the deeper part of the limestone.

Cluster 5 is also sensitive to water-excess presenting with a median resistivity of 1649 Ω·m, with a range between 1432 Ω·m to 2635 Ω·m (Figure 6B). The time lag between cluster 5 and water-excess appears slightly higher than for sub-surface

clusters 2 and 4 (Figures 6A and 6B). However, the variability of water saturation in cluster 3 over time is basically the same in cluster 5 (Figure 6B). We suggest that cluster 5 likely corresponds to the Bajocian and Bathonian limestone, where seasonal variation may be due to water filling or draining of the fissure network.

Cluster 3, with a median resistivity value of 941 Ω·m, ranging from 775 Ω·m to 1763 Ω·m, is located at the same altitude (165-178 m, NGF) as cluster 5 (Figures 6B & 2B). Similarly, cluster 3 also experiences only a few days or one month of time delay with water-excess (Figure 6B). One observation worth mentioning is that cluster 3 has a lower median resistivity value than cluster 5, indicating a comparatively higher porosity (Figure 6B). Moreover, the drilling was carried out above the cluster 3 (at 9.5 m on the profile sees Figure 2B), showing a weathered limestone (blocks of limestone). Based on the above observation, we can conclude that cluster 3 acts as a preferred water pathway due to its higher porosity, functioning as a transmission belt (located on the right side of Figure 2B), which supplies water to deeper zones linked to cluster 6.

Cluster 1 has a median resistivity value of 3040 Ω·m, ranging from 2321 Ω·m to 4957 Ω·m (Figure 7A), a higher resistivity value than cluster 5 (1649 Ω·m). Cluster 1 is mainly distributed around the cave gallery and along the 10-50 m section of the ERT profile (at an altitude of 176 m-178 m, NGF) (Figure 2B). Cluster 1 resistivity increases in summer/autumn and decreases in winter/spring, basically in the same pattern or ahead of the cave dripping rate (Vil-#10A) (Figure 3A). We observed a time delay of about 1-2 months for cluster 1 in response to local water-excess (Figure 7A). This delay may be associated with the percolation threshold between water-excess and drip rate as described in section 4.3 (Figure 3; Figure 7A). Bulk resistivity is directly inversely proportional to the conductivity of the water based on Archie's law, called the "water conductivity effect" (Archie, 1942). However, the field monitoring conducted in earlier research between 1996 and 1997 shows that the electrical conductivity of the water varied slightly, and was around 356 µS/cm (summer months) and 372 µS/cm (winter months) at station Vil-#10A (cluster 1) in the upper gallery (Baker et al., 2000; Genty et al., 2001). Consequently, based on the

observations and results obtained in Vil-#10A, it can be concluded that the upper gallery does not exhibit any significant "water conductivity effect", as water conductivity of the water in this zone remains stable and does not change with time.

Cluster 6, located at the lowest altitudes of the ERT profiles, has a median resistivity value of 808 Ω·m, ranging from 493 Ω·m to 1133 Ω·m. Resistivity values in cluster 6 are lower than in cluster 5 (1649 Ω·m) (Figure 7B), suggesting higher water content. In wet periods, cluster 6 median resistivity displayed seasonal variability linked to water excess, but it appeared to be far more time delayed to water-excess than other clusters (Figure 7B). However, there were two long-term inconsistent excursions with water-excess in the dry periods (May-October 2020 and April-October, 2022), especially in summer (Figure 7B). Unlike cluster 1, the resistivity of cluster 6, situated in the deeper sections of the profiles (below 165 m NGF), appeared to be predominantly influenced by the "water conductivity effect" in the dry/summer periods (Archie, 1942). Water conductivity in the lower gallery station Vil-#1B, which is situated close to the altitude of cluster 6, is higher and varied seasonally from 600 µS/cm (summer months) to 460 µS/cm (winter months) (Baker et al., 2000; Genty et al., 2001). The resistivity variability in cluster 6 is interpreted as the outcome of a "piston flow" infiltration system, wherein the infiltration water conductivity increased significantly during summer/dry periods due to its prolonged residence time, resulting in intensified mineralization within fissures and micro-fissures.

By comparing the ERT's seasonal signal changes with rainfall data (input) and drip rate data (output), we estimated the inertia of the reservoir inertia and identified the fast-response zones in clusters 2-4 and the delay times in cluster 1 (1-2 month). We also confirmed that clusters 3 and 2.1 are pathway of water flux pathways. ERT images were used to determine changes in the reservoirs (number, location, depth, size) and their water saturation, which can be linked to cave hydrological signatures (drip rate changes).

5.2. Schematic diagram of the unsaturated karst zone around Villars Cave

In view of the geophysical analysis and hydrological knowledge of the studied region, we developed a schematic geo-electrical synthetic model (Figure 8). The boundaries in the geo-electrical structure's boundaries are inferred from the HAC method (Figure 2B). The model delineates the limestone, top-soil, weathered limestone, privileged feeding zone, and storage zones based on their resistivity values and temporal resistivity variations linked to cave water drip rate (Figures 5, 6, and 7)

From this synthetic image, it is possible to draw a schematic diagram of the groundwater movement pathways in the critical karstic zone (KCZ) above the Villars Cave (Figure 8). We can speculate that the most of the water flow originates from the soil layers and inter-connected epikarst reservoirs, and subsequently, it moves deeper into the porous limestone zone (cluster 3). However, precipitation can also infiltrate vertically through fracture networks in the Bajocian and Bathonian limestone (cluster 5, Figure 4). The rapid water circulation observed in cluster 2 is highly sensitive to local rainfall, which is compounded with the superficial top soil and weathered limestone areas mixed with sand at the surface and between 50-60 m (altitude: 172 m to 177 m, NGF) of the ERT profile (Figure 8).

Regarding storage zones in Villars, cluster 6 is able to act as a water reservoir from a fast fissure network transport of water in cluster 5 and the transport of water from cluster 3 and cluster 2.1 (Figure 8). Similarly, it appears that cluster 1 also acts as a storage zone with a hydrological behavior closely linked to the dripping rate in the upper gallery (Vil-#10A) (Figure 7A). Cluster 1 stores local rainwater and regulate its release over time, with potentially significant implications for feeding upper gallery stalagmites in the Villars Cave.

To summarize, the cluster characteristics and behaviors are not randomly distributed but they highlight the structures of the infiltration zone which can be interpreted as reservoirs, or preferential rapid or slow infiltration zones. By testing

555 and validating ERT and hydrology methods at a specific site (Villars Cave) developed
556 in a vadose zone, we can deepen our understanding of the site and its hydrological
557 behavior, which may be similar to other caves in the region. This can give us more
558 insights into the hydrogeological and hydrological processes in the karst environment
559 and improve our ability to manage and protect these sensitive karst environments.

560 # 6. Conclusions

561 Long-term monitoring of the karst vadose zone above the Villars Cave in SW-
562 France, involving 2.5 years of ERT data combined with drip rate measurements inside
563 the cave, has provided valuable insights into the geometry and dynamics of aquifer
564 recharge processes. By employing the Hierarchical Agglomerative Clustering (HAC)
565 method on ERT images, distinct clusters (clusters 1 to 8) were identified, exhibiting
566 different resistivity zones linked to dripping water sources within the Villars Cave.
567 Below are the main conclusions drawn from the study:

568 (1) Clusters 2 and 4, located in the superficial layer of ERT profiles, correspond
569 to the top soil (clusters 4 and 2.2) and slightly deeper weathered limestone
570 (cluster 2.1). Resistivity variations in these clusters directly relate to
571 changes in water-excess and local drought period.

572 (2) Cluster 5, situated in the middle layers of the ERT images, exhibits
573 pronounced seasonal resistivity changes. The cluster presents short delay
574 with water-excess variations, likely attributed to the filling or draining of
575 fissures and micro-fissures.

576 (3) Cluster 3, predominantly located on the right side of the ERT images and
577 characterized by slightly lower resistivity, appears to act as a preferential
578 infiltration pathway moving to deeper reservoirs. Like cluster 5, cluster 3
579 also demonstrates a delay of a few days or one month after water-excess.

580 (4) Cluster 6, located in the deeper part of the ERT profile, displays seasonal
581 variability in resistivity during wet periods but exhibits low resistivity
582 values during summer or dry periods. This behavior is likely due to the

presence of mineralized infiltration waters.

(5) Cluster 1, distributed around the cave galleries, consists of high-resistivity limestone and is connected to the cave dripping hydrology. This cluster exhibits a delay of 1-2 months with respect to water excess, suggesting the presence of a percolation threshold that supplies water to the cave stalagmites in Villars.

(6) Clusters 7 and 8 exhibit extremely high resistivity values without any seasonal changes. These areas coincide with the cave galleries or sinkhole collapses.

By conducting a comprehensive analysis that combines ERT results and drip water measurements, we can effectively characterize the origins of drip rate signals in cave systems. This integrated approach provides valuable insights into the hydrodynamic behavior of water flow and the lithological/geological constraints present in the karst subsurface. Establishing direct links between changes in subsurface resistivity and dynamic water percolation processes within the cave environment, our in-depth understanding of the hydrogeological processes contributes significantly to the management and conservation of water resources in karst regions, helping to develop sustainable water use and environmental protection. The approach not only provides a novel and promising method for studying different flow types and their origins in caves but also enhances our understanding of karst aquifer recharge processes, which is vital for cave and paleoclimate studies.

Acknowledgments

We thank the Versaveaud family, who are always interested in our research, and their constant help makes the long-term monitoring work in Villars Cave possible. We want to express sincere thanks to Olivier Mestre for the help with meteorological data. We thank Thierry Baritaud for his help in data collecting and field trips. We thank Daniel Chailloux, Laurent Magne, Gilles Souchet for their help in determining the drip sites. This work was supported by I2M programs on decorated caves for geophysical surveys and thermal monitoring. This research was also supported by the

China Scholarship Council (CSC) to Jian. Zhang (201906990014). This long monitoring work (DG) has been funded, since 1996, by several programs from the CNRS (INSU), and three laboratories (GEOPS, Orsay, Paris-Saclay University; Laboratoire des Sciences du Climat et de l'Environnement, LSCE, CEA/CNRS/UVSQ and Environnements et Paléoenvironnements Océaniques et Continentaux, EPOC, University of Bordeaux, France). Villars Cave is part of the sites that are studied by the CNRS GIS group called GEMS "Groupe d'Etude des Milieux Souterrains", dir. B. Lartiges GET Toulouse". Department of Environmental Sciences, University of Bordeaux, financially supports this project.

CRediT authorship contribution statement

Jian Zhang: Conceptualization, Methodology, Formal analysis, Writing - review & editing. **Colette Sirieix:** Supervision, Revising and editing, Reviewing, Funding acquisition. **Dominique Genty:** Review & editing, Supervision, Funding acquisition, Dripping monitoring data. **Cecile Verdet, Marie Larcanche and Shan Xu:** Software and data analysis, **Fabien Salmon:** Thermal model, **Sylvain Mateo:** Geophysical Field works**, Stéphane Bujan** and **Ludovic Devaux:** Field works.

Declaration of Competing Interest

The authors declare that they have no known competing financial interests or personal relationships that could have appeared to influence the work reported in this paper.

References

Al Hagrey, S.A., 2007. Geophysical imaging of root-zone, trunk, and moisture heterogeneity. J. Exp. Bot. 58 (4), 839–854. https://doi.org/10.1093/jxb/erl237.

Archie, G. 1942. The electrical resistivity log as an aid in determining some reservoir characteristics. Petroleum Transactions of the AIME, 146, 54-62. https://doi.org/10.2118/942054-G

Baker, A., Genty, D., & Fairchild, I. J. 2000. Hydrological characterisation of stalagmite dripwaters at Grotte de Villars, Dordogne, by the analysis of inorganic species and

luminescent organic matter. Hydrol. Earth Syst. Sci., 4, 439–449, https://doi.org/10.5194/hess-4-439-2000, 2000.

Barker, R., Moore, J., 1998. The application of time-lapse electrical tomography in groundwater studies. Lead. Edge 17 (10), 1454–1458. https://doi.org/10.1190/ 1.1437878.

Besson, A., Cousin, I., Dorigny, A., Dabas,M., King, D., 2008. The temperature correction for the electrical resistivity measurements in undisturbed soil samples: analysis of the existing conversion models and proposal of a new model. Soil Sci. 173, 707–720. DOI: 10.1097/SS.0b013e318189397f

Binley, A., Hubbard, S. S., Huisman, J. A., Revil, A., Robinson, D. A., Singha, K., & Slater, L. D. 2015. The emergence of hydrogeophysics for improved understanding of subsurface processes over multiple scales. Water Resour. Res., 51(6), 3837-3866. https://doi.org/10.1002/2015WR017016

Brunet, P., Clement, R., Bouvier, C., 2010. Monitoring soil water content and deficit using Electrical Resistivity Tomography (ERT)–A case study in the Cevennes area. France. J. Hydrol. 380 (1), 146–153. https://doi.org/10.1016/j. jhydrol.2009.10.032.

Carriere, S.D., Chalikakis, K., S´en´echal, G., Danquigny, C., Emblanch, C., 2013. Combining electrical resistivity tomography and ground penetrating radar to study geological structuring of karst unsaturated zone. J. Appl. Geophys. 94, 31–41. ht tps://doi.org/10.1016/j.jappgeo.2013.03.014.

Caterina, D., Orozco, A. F., & Nguyen, F. 2017., Long-term ERT monitoring of biogeochemical changes of an aged hydrocarbon contamination. J. Contam. Hydrol.201, 19-29. https://doi.org/10.1016/j.jconhyd.2017.04.003

Chalikakis, K., Plagnes, V., Guerin, R., Valois, R., & Bosch, F. P. 2011., Contribution of geophysical methods to karst-system exploration: an overview. Hydrogeol. J., 19(6), 1169-1180. DOI: 10.1007/s10040-011-0746-x

Chambers, J. E., Gunn, D. A., Wilkinson, P. B., Meldrum, P. I., Haslam, E., Holyoake, S., Kirkham, M., Kuras, O., Merritt, A., and Wragg, J.: 4-D electrical resistivity tomography monitoring of soil moisture dynamics in an operational railway embankment, Near Surf. Geophys., 12, 61–72, https://doi.org/10.3997/1873-0604.2013002, 2014.

Chen, X., Zhang, Z., Soulsby, C., Cheng, Q., Binley, A., Jiang, R. , et al. 2018. Characterizing the heterogeneity of karst critical zone and its hydrological function: an integrated approach. Hydrol. Process., 32(19), 2932-2946. https://doi.org/10.1002/hyp.13232

Coscia, I., Linde, N., Greenhalgh, S., Günther, T., and Green, A.: A filtering method to correct time-lapse 3-D ERT data and improve imaging of natural aquifer dynamics, J. Appl. Geophys., 80, 12–24, https://doi.org/10.1016/j.jappgeo.2011.12.015, 2012.

De Carlo, L.; Perkins, K.; Caputo, M.C. 2021. Evidence of preferential flow activation in the vadose zone via geophysical monitoring. Sensors 21, 1358. https://doi.org/10.3390/s21041358

Delgado-Gonzalez, L., Forquet, N., Choubert, J.M., Boutin, C., Moreau, M., Moreau, S. and

678
679
680
Clement, R., 2023. Flow path monitoring by discontinuous time-lapse ERT: An application to survey relationships between secondary effluent infiltration and roots distribution. J. Environ. Manage., 326, p.116839. https://doi.org/10.1016/j.jenvman.2022.116839

681
682
Ford, D.C. and Williams, P. 2007. Karst Hydrogeology and Geomorphology. John Wiley, Chichester, 562.

683
684
685
686
Gautam, P., Pant, S.R. Ando, H., 2000. Mapping of subsurface karst structure with gamma ray and electrical resistivity profiles: a case study from Pokhara valley, central Nepal. J. Appl. Geophys., 45/2: 97-110. https://doi.org/10.1002/ 9781118684986 Geotest user manual 2.50, Available from: http://www.geophysik-dr-rauen.de. Nov 2019.

687
688
689
Genelle, F., Sirieix, C., Riss, J., & Naudet, V. 2012., Monitoring landfill cover by electrical resistivity tomography on an experimental site. Eng. Geol., 145, 18-29. https://doi.org/10.1016/j.enggeo.2012.06.002

690
691
Genty, D., Baker, A., & Vokal, B. 2001. Intra-and inter-annual growth rate of modern stalagmites. Chem. Geol., 176(1-4), 191-212. https://doi.org/10.1016/S0009-2541(00)00399-5

692
693
694
Genty, D., Blamart, D., Ouahdi, R., Gilmour, M., Baker, A., Jouzel, J., & Van-Exter, S. 2003. Precise dating of Dansgaard–Oeschger climate oscillations in western Europe from stalagmite data. Nature, 421(6925), 833. https://doi.org/10.1038/nature01391

695
696
697
698
699
Genty. D., Blamart. D., Ghaleb. B., Plagnes. V., Causse. C., Bakalowicz. M., Zouari. K., Chkir.N., Hellstrom. J., Wainer. K., Bourges. F., 2006. Timing and dynamics of the last deglaciation from European and North African delta C-13 stalagmite profiles – comparison with Chinese and South Hemisphere stalagmites. Quatern. Sci. Rev. 25, 2118–2142. https://doi.org/10.1016/j.quascirev.2006.01.030

700
701
Genty. D., 2008. Palaeoclimate research in Villars Cave (Dordogne, SW-France). Int. J. Speleol. 37, 173–191. https://digitalcommons.usf.edu/ijs/vol37/iss3/3

702
703
704
705
Genty, D., Labuhn, I., Hoffmann, G., Danis, P.A., Mestre, O., Bourges, F., Wainer, K., Massault, M., Van Exter, S., Régnier, E., Orengo, Ph., Falourd, S., Minster, B., 2014. Rainfall and cave water isotopic relationships in two South-France sites. Geochim. Cosmochim. Acta. 131 (5), 323–343. https://doi.org/10.1016/j.gca.2014.01.043

706
707
708
Hartmann, A., Baker, A., 2017. Modelling karst vadose zone hydrology and its relevance for paleoclimate reconstruction. Earth-Sci. Rev. 172, 178–192.https://doi.org/10.1016/j.earscirev.2017.08.001.

709
710
711
Hayley, K., Bentley, L. R., Gharibi, M., & Nightingale, M. 2007. Low temperature dependence of electrical resistivity: Implications for near surface geophysical monitoring. Geophys. Res. Lett., 34(18). https://doi.org/10.1029/2007GL031124

712
713
714
Hermans, T., Nguyen, F., Robert, T., & Revil, A. 2014. Geophysical methods for monitoring temperature changes in shallow low enthalpy geothermal systems. Energies, 7(8), 5083-5118. https://doi.org/10.1007/s10040-011-0819-x, 2012.

715
Kadam, A.K., Patil, S.N., Gaikwad, S.K. et al. Demarcation of subsurface water storage potential

zone and identification of artificial recharge site in Vel River watershed of western India: integrated geospatial and hydrogeological modeling approach. Model. Earth Syst. Environ. (2023). https://doi.org/10.1007/s40808-022-01656-4

Kaufmann, O. and Deceuster, J. 2014. Detection and mapping of ghostrock features in the Tournaisis area through geophysical methods– an overview, Geol. Belg., 17, 17–26, https://popups.uliege.be/1374-8505/index.php?id=4130.

Keller, G.V., Frischknecht, F.C., 1966. Electrical Methods in Geophysical Prospecting. Pergamon Press, Oxford, UK, pp. 30–33.

Kuras, O., Pritchard, J. D., Meldrum, P. I., Chambers, J. E., Wilkinson, P. B., Ogilvy, R. D., and Wealthall, G. P. 2009., Monitoring hydraulic processes with automated time-lapse electrical resistivity tomography (ALERT), C. R. Geosci., 341, 868–885, https://doi.org/10.1016/j.crte.2009.07.010

LaBrecque, D. J., Ramirez, A. L., Daily, W. D., Binley, A. M., and Schima, S. A. 1996.: ERT monitoring of environmental remediation processes, Meas. Sci. Technol., 7, 375, 1996. DOI 10.1088/0957-0233/7/3/019

Lacanette, D., Malaurent, P., Caltagirone, J.P., Brunet, J., 2007. Etude des transferts de masse et de chaleur dans la grotte de Lascaux. Karstologia 50, 19–30. DOI : https://doi.org/10.3406/karst.2007.2608

Leopold, M., Gupanis-Broadway, C., Baker, A., Hankin, S., & Treble, P. 2021. Time lapse electric resistivity tomography to portray infiltration and hydrologic flow paths from surface to cave. J. Hydrol., 593, 125810. https://doi.org/10.1016/j.jhydrol.2020.125810

Lharti, H., Sirieix, C., Riss, J., Verdet, C., Salmon, F., & Lacanette, D. 2023. Partitioning a rock mass based on electrical resistivity data: the choice of clustering method. Geophysical Journal International, 2023, ggad081, https://doi.org/10.1093/gji/ggad081

Ma, R.J., McBratney, A., Whelan, B., Minasny, B., Short, M., 2011. Comparing temperature correction models for soil electrical conductivity measurement. Precis. Agric. 12, 55–66. https://doi.org/10.1007/s11119-009-9156-7

Meyerhoff, S. B., Karaoulis, M., Fiebig, F., Maxwell, R. M., Revil, A., Martin, J. B., and Graham, W. D.: 2012. Visualization of conduit-matrix conductivity differences in a karst aquifer using time-lapse electrical resistivity: ERT time-lapse of karst conductivity, Geophys. Res. Lett., 39, L24401, https://doi.org/10.1029/2012GL053933., 2012.

Michot, D., Benderitter, Y., Dorigny, A., Nicoullaud, B., King, D., Tabbagh, A., 2003. Spatial and temporal monitoring of soil water content with an irrigated corn crop cover using surface electrical resistivity tomography. Water Resour. Res. 39/5 https://doi.org/10.1029/2002WR001581

Pakzad, L., Ein-Mozaffari, F., Chan, P., 2008. Using electrical resistance tomography and computational fluid dynamics modeling to study the formation of cavern in the mixing of pseudoplastic fluids possessing yield stress. Chem. Eng. Sci. 63 (9), 2508–2522. https://doi.org/10.1016/j.ces.2008.02.009.

Peter ‐ Borie, M., Sirieix, C., Naudet, V., Riss, J. 2011. Electrical resistivity monitoring with buried electrodes and cables: noise estimation with repeatability tests. Near Surf. Geophys., 9(4), 369-380. DOI: https://doi.org/10.3997/1873-0604.2011013

Pope, G.G., Nyquist, J.E., Toran, L., 2023. Time-Lapse Resistivity Monitoring of a Simulated Runoff Test in a Bioswale, Philadelphia. J. Sustain. Water Built Environ. 9, 04022018. https://doi.org/10.1061/JSWBAY.0001003.

Revil, A., Karaoulis, M., Johnson, T., and Kemna, A.2012.: Review: some low-frequency electrical methods for subsurface characterization and monitoring in hydrogeology, Hydrogeol. J., 20, 617–658, DOI:10.1007/s10040-011-0819-x

Robert, T., Dassargues, A., Brouy`ere, S., Kaufmann, O., Hallet, V., Nguyen, F., 2011. Assessing the contribution of electrical resistivity tomography (ERT) and self-potential (SP) methods for a water well drilling program in fractured/karstified limestones. J. Appl. Geophys. 75 (1), 42–53. https://doi.org/10.1016/j. jappgeo.2011.06.008.

Salmon, F., Lacanette, D., Lharti, H., Sirieix, C., 2023. Heat Transfer in Rock Masses: Application to the Lascaux Cave (France). Int. J. Heat Mass Transf., 207, 124029. https://doi.org/10.1016/j.ijheatmasstransfer.2023.124029

Samouëlian, A., Cousin, I., Tabbagh, A., Bruand, A., and Richard, G.: Electrical resistivity survey in soil science: a review, Soil Till. Res., 83, 173–193, https://doi.org/10.1016/j.still.2004.10.004, 2005.

Saporta, G., 1990. Probabilités et analyse des données, et Statistique. Editions Technip, Paris (493 pp.).

Sirieix, C., Riss, J., Rey, F., Prétou, F., Lastennet, R., 2014. Electrical resistivity tomography to characterize a karstic spring Vauclusian: Fountain Orbe (Pyrenees, France). Hydrogeol. J. 22 (4):911–924. http://dx.doi.org/10.1007/s10040-013-1095-8.

Song, S.Y., Kim, B., Jeong, J. et al. 4D interpretation of time-lapse electrical resistivity monitoring data to identify preferential flow path in a landfill, South Korea. Environ Monit Assess 195, 625 (2023). https://doi.org/10.1007/s10661-023-11149-1

Telford, W.M., Geldart, L.P. and Sheriff, R.E., 1990. Applied Geophysics (second edition). Cambridge University Press.

Torrese, P. 2020., Investigating karst aquifers: Using pseudo 3-D electrical resistivity tomography to identify major karst features. J. Hydrol, 580, 124257. https://doi.org/10.1016/j.jhydrol.2019.124257

Uhlemann, S.S., Sorensen, J.P.R., House, A.R., Wilkinson, P.B., Roberts, C., Gooddy, D.C., Binley, A.M., Chambers, J.E., 2016. Integrated time-lapse geoelectrical imaging of wetland hydrological processes. Water Resour. Res. 52 (3), 1607–1625. https://doi.org/10.1002/2015WR017932.

Uhlemann, S.S., Kuras, O., Richards, L.A., Naden, E., Polya, D.A., 2017. Electrical resistivity tomography determines the spatial distribution of clay layer thickness and aquifer vulnerability,

Kandal Province, Cambodia. J. Asian Earth Sci Advance online publication. https://doi.org/10.1016/j.jseaes

Vacher, H.L., Mylroie, J.E., 2002. Eogenetic karst from the perspective of an equivalent porous medium. Carbonates Evaporites 17 (2), 182–196. https://doi.org/10.1007/ BF03176484.

Valois, R., Bermejo, L., Gu´erin, R., Hinguant, S., Pigeaud, R., Rodet, J., 2010. Karstic morphologies identified with geophysics around Saulges caves (Mayenne, France). Archaeol. Prospect. 17, 151–160. https://doi.org/10.1002/arp.385.

Vanderborght, J., Kemna, A., Hardelauf, H., Vereecken, H., 2005. Potential of electrical resistivity tomography to infer aquifer transport characteristics from tracer studies: A synthetic case study. Water Resour. Res. 41/6 https://doi.org/10.1029/ 2004WR003774.

Verdet, C., Sirieix, C., Marache, A., Riss, J., & Portais, J. C. 2020. Detection of undercover karst features by geophysics (ERT) Lascaux cave hill. Geomorphology, 360, 107177. https://doi.org/10.1016/j.geomorph.2020.107177.

Wainer K., Genty D., Blamart D., Hofmann D., Couchoud I., 2009, A new stage 3 millennial climatic variability record from a SW France speleothem, Palaeogeogr., Palaeoclim., Palaeoecol., 271: 130-139. https://doi.org/10.1016/j.palaeo.2008.10.009

Wainer K., Genty D., Blamart D., Daëron M., Bar-Matthews M., Vonhof H., Dublyansky Y., Pons-Branchu E., Thomas L., van Calsteren P., Quinif Y. and Caillon N., 2011, Speleothem record of the last 180 ka in Villars cave (SW France): Investigation of a large $\delta^{18}O$ shift between MIS6 and MIS5, Quatern. Sci. Rev., 30:130-146. https://doi.org/10.1016/j.quascirev.2010.07.004.

Wainer K., Genty D., Blamart D., Bar-Matthews M., Quinif Y., Plagnes V., 2013, Millennial climatic instability during penultimate glacial period recorded in a south-western France speleothem., Palaeogeogr., Palaeoclim., Palaeoecol., 376:122-131. https://doi.org/10.1016/j.palaeo.2013.02.026.

Watlet, A., Kaufmann, O., Triantafyllou, A., Poulain, A., Chambers, J.E., Meldrum, P.I., Wilkinson, P.B., Hallet, V., Quinif, Y., Van Ruymbeke, M., Van Camp, M., 2018. Imaging groundwater infiltration dynamics in the karst vadose zone with long-term ERT monitoring. Hydrol. Earth Syst. Sci. 22, 1563–1592. https://doi.org/10.5194/ hess-22-1563-2018.

White,W. B. 2002., Karst hydrology: recent developments and open questions, Eng. Geol., 65, 85–105, https://doi.org/10.1016/S0013-7952(01)00116-8

Williams, P. W. 2008. The role of the epikarst in karst and cave hydrogeology: a review, Int. J. Speleol., 37, 1–10., https://digitalcommons.usf.edu/kip_articles/4687

Xu, S., Sirieix, C., Ferrer, C., Lacanette-Puyo, D., Riss, J., Malaurent, P., 2015. A geophysical tool for the conservation of a decorated cave. - a case study for the Lascaux cave. Archaeol. Prospect. http://dx.doi.org/10.1002/arp.1513 (online in Wiley Online Library).

Xu, S., Sirieix, C., Marache, A., Riss, J., Malaurent, Ph., 2016. 3D geostatistical modeling of Lascaux hill from ERT data. Eng. Geol. 213 (4):169–178. http://dx.doi.org/10.1016/j.

enggeo.2016.09.009.

Xu, S., Sirieix, C., Riss, J., and Malaurent, P. 2017.: A clustering approach applied to time-lapse ERT interpretation – case study of Lascaux cave, J. Appl. Geophys., 144, 115–124, ht tps://doi.org/10.1016/j.jappgeo.2017.07.006., 2017.

Yan, Y., Deng, Y., Ma, L. 2023. Characterizing seasonal recharge between a river and shallow aquifer in a floodplain based on time-lapse electrical resistivity tomography. Hydrogeol. J 31, 111-126. https://doi.org/10.1007/s10040-022-02574-6

Zenone, T., Morelli, G., Teobaldelli, M., Fischanger, F., Matteucci, M., Sordini, M., Armani, A., Ferr`e, C., Chiti, T., Seufert, G., 2008. Preliminary use of ground-penetrating radar and electrical resistivity tomography to study tree roots in pine forests and poplar plantations. Funct. Plant Biol. 35 (10), 1047–1058. https://doi. org/10.1071/FP08062.

Zhang, J., Genty, D., Sirieix, C., Michel, S., Minster, B., Regnier, E., 2020. Quantitative assessment of moisture source and temperature governing rainfall $\delta^{18}O$ from 20 years-long monitoring records in SW-France: importance for isotopic-based climate reconstructions. J. Hydrol. 591, 1-20. https://doi.org/10.1016/j.jhydrol.2020.125327

Zhou, W., Beck, B.F., Adams, A.L., 2002. Effective electrode array in mapping karst hazards in electrical resistivity tomography. Environ. Geol. 42 (8), 922–928. https:// doi.org/10.1007/s00254-002-0594-z.

Caption

Figure 1. **(A)** Location of the Villars Cave. **(B)** A 3D structural cave diagram and the distribution of monitoring sites (red circles): Vil-#3, Vil-#1B, Vil-#10A. The reader is referred to (Genty, 2008 and Genty et al., 2014) for detailed site descriptions and maps. **(C)** Localization of ERT profiles above the Villars Cave map. The red line indicates the ERT profile we monitored for 2.5 years. The dotted circles Zone A-C correspond to the ERT image identified three cave galleries in Figure 3B. **(D)** A structural diagram and the distribution of surveillance sites of the Villars Cave (Vil-#1B, Vil-#10A, and Vil-3#). The red square shows the profile of ERT. The drip points Vil-#1B and Vil-#3 are about 5 m apart, located on the lower level of the cave while the drip points Vil-#10A are located on the upper level of the cave. This section clearly shows that Stations Vil-#1B and Vil-#3 are at the same altitude as the Trincou stream.

862

863 **Figure 2.** Results of the Hierarchical Agglomerative Classing (HAC) for all
864 monitoring periods for the profile (71m) above the Villars Cave. **(A)** Dendrogram to
865 create three and eight clusters. **(B)** Distribution of blocks considering their clusters.
866 Clusters 7 and 8 correspond to the high-resistivity zones identified on the Zone A-C in
867 cave plan map in Figure 1C.

868

869 **Figure 3.** Comparison of the variability of daily R-ETP (rainfall minus
870 evapotranspiration) and drip-water rates (Vil-#3, Vil-#1B, Vil-#10A) during
871 September/2019- September/2022. Water-excess (rainfall-evapotranspiration > 0).

872

873 **Figure 4. (A)** Cluster 2 is divided into clusters 2.1 and 2.2 blocks, **(B)** Comparisons
874 between median resistivity variations for clusters 2.1 and 2.2 and water excess.

875

876 **Figure 5.** Evolutions of the median resistivity of clusters 1-8 with local water-excess.
877 The individual blocks from the synthetic model were associated with a similar
878 seasonal resistivity variability gathered into 6 clusters (1-6). However, clusters 7 and
879 8 only exhibit a high resistivity without an obvious seasonal variability. The arrows
880 indicated the decrease in resistivity in cluster 6 in the dry/summer periods.

881

882 **Figure 6. (A)** Evolutions of the median resistivity of clusters 2 and 4 with local water
883 -excess **(B)** Evolutions of the median resistivity of clusters 3 and 5 with local water-
884 excess. A similar seasonally variable resistivity was found in 4 clusters (2-5) with no
885 or few days of delay with local water excess.

886

887 **Figure 7. (A)** Evolutions of the median resistivity of cluster 1. **(B)** Evolutions of the
888 median resistivity of cluster 6. Dashed lines indicate the point at which resistivity and
889 water excess and drip rate begin to increase in response to a delay in the percolation
890 threshold. The red dotted area is affected by water conductivity.

891

892 **Figure 8.** Schematic geo-electrical model of the ERT survey line. The wiggle arrows
893 represent preferential flow, and the straight arrows represent vertical flow in the pipe
894 and fissure.

895

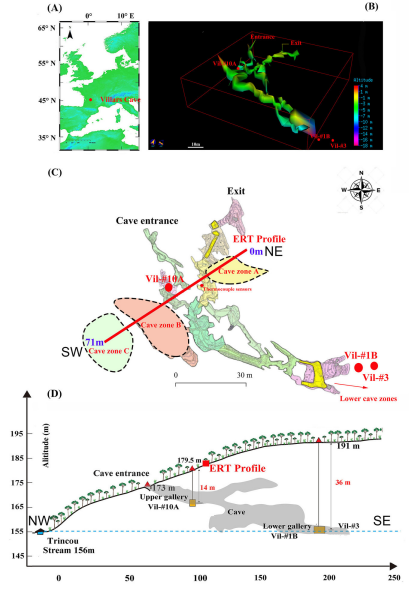
(A)
0°
10° E
65° N
55° N
45° N
35° N
Vil-#10A
Zone
(B)
Entrance
Exit
Vil-#10A
Vil-#1B
Vil-#3
RTI/Code
(C)
N
W
E
S
Exit
Cave entrance
ERT Profile
0m NE
Vil-#10A
Cave zone A
Speleothem zones
Cave zone B
SW 171m
Cave zone C
Vil-#1B
Vil-#3
Lower cave zones
0
30 m
(D)
Altitude (m)
195
185
175
165
155
145
Cave entrance
179.5 m
ERT Profile
191 m
36 m
14 m
173 m
Upper gallery
Vil-#10A
Cave
NW 0m
SE
Lower gallery
Vil-#1B
Vil-#3
Trincou
Stream 156m
0
50
100
150
200
250

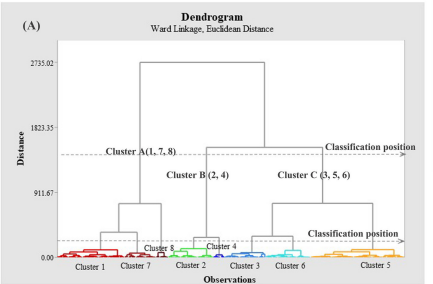
(A)
Dendrogram
Ward Linkage, Euclidean Distance
2735.02
1823.35
911.67
0.00
Distance
Cluster A(1, 7, 8)
Classification position
Cluster B (2, 4)
Cluster C (3, 5, 6)
Classification position
Cluster 8
Cluster 4
Cluster 1
Cluster 7
Cluster 2
Cluster 3
Cluster 6
Cluster 5
Observations

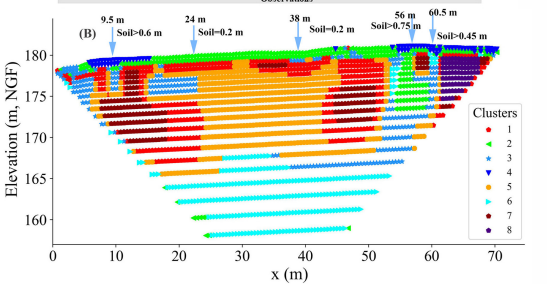
(B)
9.5 m
Soil>0.6 m
24 m
Soil=0.2 m
38 m
Soil=0.2 m
56 m
Soil>0.75 m
60.5 m
Soil>0.45 m
Elevation (m, NGF)
180
175
170
165
160
0
10
20
30
40
50
60
70
x (m)
Clusters
1
2
3
4
5
6
7
8

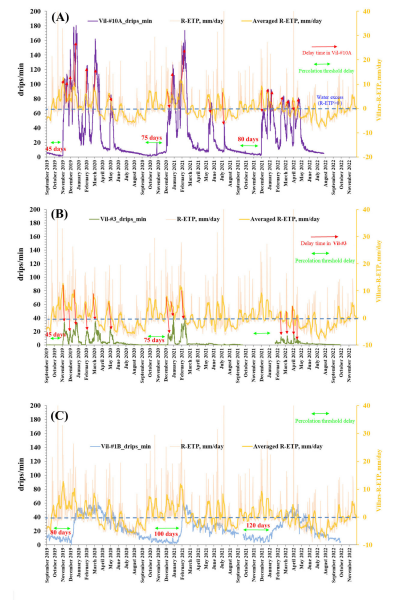
(A)
VII-910A_drips_min
R-ETP, mm/day
Averaged R-ETP, mm/day
drips/min
Vflux R-ETP, mm/day
Delay time in VII-910A
Percolation threshold delay
None ongoing (R-ETP<0)
45 days
75 days
80 days
(B)
VII-93_drips_min
R-ETP, mm/day
Averaged R-ETP, mm/day
drips/min
Vflux R-ETP, mm/day
Delay time in VII-93
Percolation threshold delay
35 days
75 days
(C)
VII-91B_drips_min
R-ETP, mm/day
Averaged R-ETP, mm/day
drips/min
Vflux R-ETP, mm/day
Percolation threshold delay
30 days
100 days
120 days

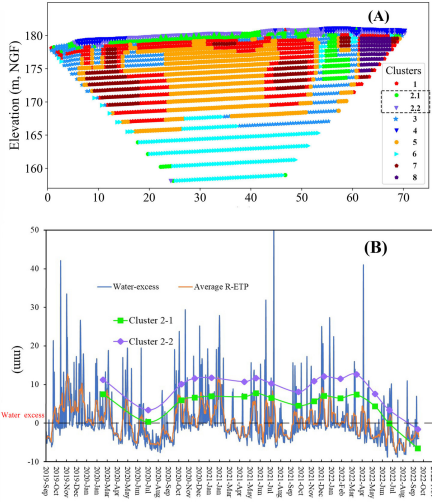
(A)
Elevation (m, NGF)
180
175
170
165
160
0
10
20
30
40
50
60
70
Clusters
2-1
2-2
3
4
5
6
7
8
(B)
Water-excess
Average R-ETP
Cluster 2-1
Cluster 2-2
(mm)
50
40
30
20
10
0
-10
Water excess
Log10 (Ω)
2
2.5
3
3.5
Resistivity (Ω·m)
100
316
1000
3162
2019-Sep
2019-Oct
2019-Nov
2019-Dec
2020-Jan
2020-Feb
2020-Mar
2020-Apr
2020-May
2020-Jun
2020-Jul
2020-Aug
2020-Sep
2020-Oct
2020-Nov
2020-Dec
2021-Jan
2021-Feb
2021-Mar
2021-Apr
2021-May
2021-Jun
2021-Jul
2021-Aug
2021-Sep
2021-Oct
2021-Nov
2021-Dec
2022-Jan
2022-Feb
2022-Mar
2022-Apr
2022-May
2022-Jun
2022-Jul
2022-Aug
2022-Sep
2022-Oct
2022-Nov
2022-Dec

Sep/2019
Dec/2019
Mar/2020
Jun/2020
Sep/2020
Dec/2020
Mar/2021
Jun/2021
Sep/2021
Dec/2021
Mar/2022
Jun/2022
Sep/2022
Dec/2022
Low
High
Low
Rainfall-ETP>0,called Water-excess
Rainfall-ETP<0
(A)
Rainfall-ETP (mm)
0
25
50
Cluster 4
(B)
ρ_i (Ω*m)
316
100
Log10 (ρ_i)
2.5
2.0
Cluster 2
(C)
1000
316
Winter/Spring
Winter Spring
Winter/Spring
Summer/Autumn
3.0
2.5
Cluster 5
(D)
2512
1585
Summer/Autumn
Summer/Autumn
3.4
3.2
Cluster 3
(E)
1585
1000
3.2
3.0
Cluster 1
(F)
3981
2512
2.8
3.6
3.4
Cluster 6
(G)
1000
631
3.0
2.8
Cluster 7&8
(H)
7943
5012
2.6
3.9
3.7
Sep/2019
Dec/2019
Mar/2020
Jun/2020
Sep/2020
Dec/2020
Mar/2021
Jun/2021
Sep/2021
Dec/2021
Mar/2022
Jun/2022
Sep/2022
Dec/2022

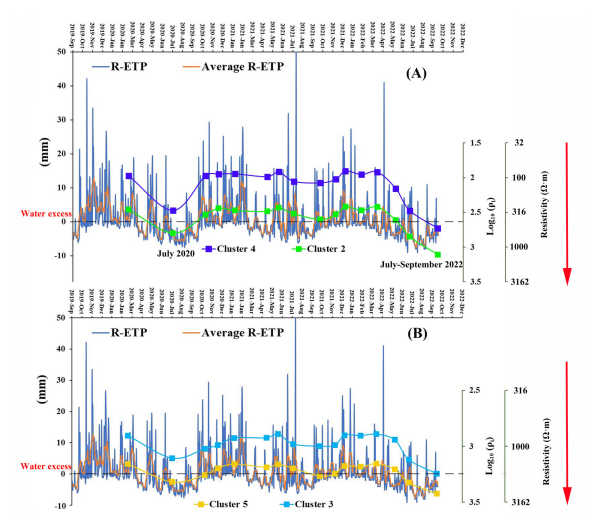
R-ETP
Average R-ETP
(A)
(mm)
Water excess
July 2020
July-September 2022
Cluster 4
Cluster 2
Log10 (ρ)
Resistivity (Ω m)
(B)
Cluster 5
Cluster 3

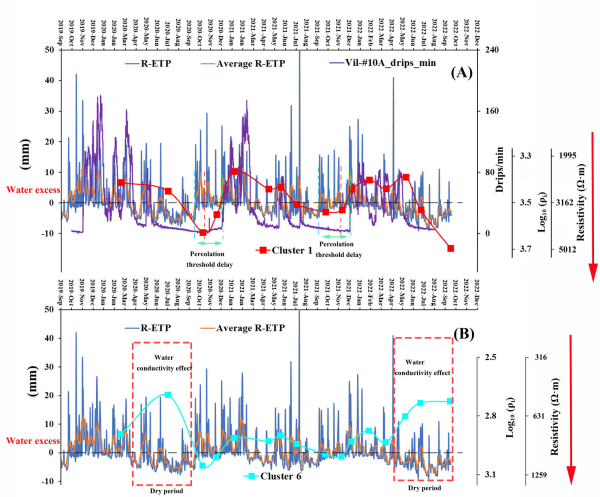
(A)
R-ETP
Average R-ETP
Vil-#10A_drips_min
(mm)
Water excess
Drips/min
Log10 (ρ)
Resistivity (Ω·m)
Percolation threshold delay
Cluster 1
(B)
Water conductivity effect
Dry period
Cluster 6

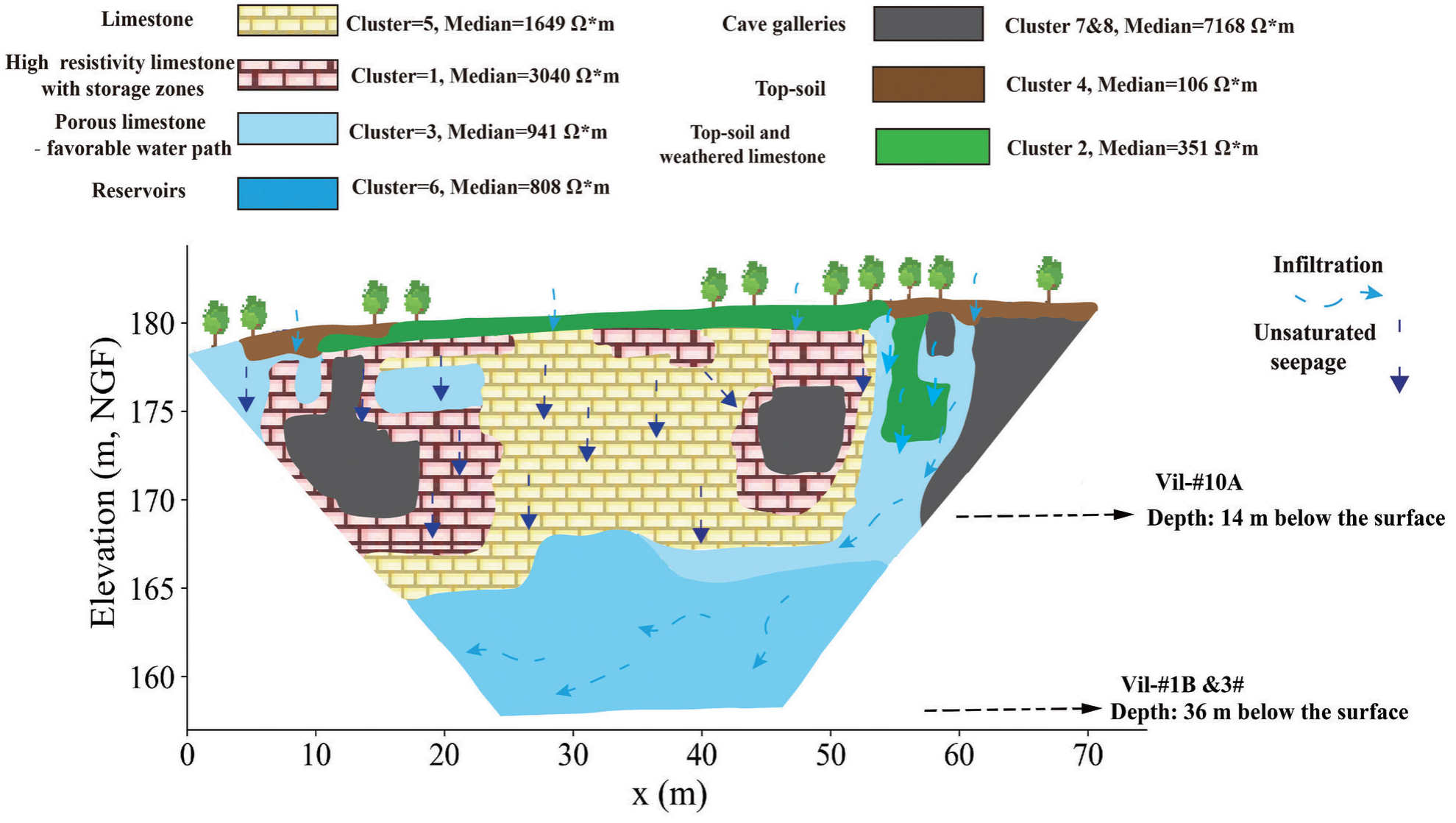
Limestone
Cluster=5, Median=1649 Ω*m
High resistivity limestone with storage zones
Cluster=1, Median=3040 Ω*m
Porous limestone - favorable water path
Cluster=3, Median=941 Ω*m
Reservoirs
Cluster=6, Median=808 Ω*m
Cave galleries
Cluster 7&8, Median=7168 Ω*m
Top-soil
Cluster 4, Median=106 Ω*m
Top-soil and weathered limestone
Cluster 2, Median=351 Ω*m
Infiltration
Unsaturated seepage
Vil-#10A
Depth: 14 m below the surface
Vil-#1B &3#
Depth: 36 m below the surface
Elevation (m, NGF)
180
175
170
165
160
0
10
20
30
40
50
60
70
x (m)

Table 1 Statistical parameters: for the resistivity of each cluster (Median and Standard Deviation (SD), Average value)

	Cluster 1			Cluster 2			Cluster 3			Cluster 4			Cluster 5			Cluster 6			Cluster 7&8		
	median	SD	average	median	SD	average	median	SD	average	median	SD	average	median	SD	average	median	SD	average	median	SD	average
2020/2/18	2592	1199	2871	289	119	299	803	262	788	94	30	90	1442	455	1565	781	194	831	8521	38310	28029
2020/7/2	2821	1481	3217	626	292	722	1277	684	1434	297	110	310	2079	666	2059	493	175	526	4610	2012	4922
2020/10/9	4249	2582	5007	342	219	390	1051	967	1405	94	35	98	1801	1087	2126	1133	343	1198	7762	36587	26594
2020/11/18	3557	1472	3596	274	195	337	979	572	1066	89	34	90	1571	767	1841	1028	682	1145	6505	29441	20534
2021/1/7	2321	988	2502	296	121	304	841	242	802	88	31	92	1440	522	1579	815	188	808	7331	13138	13553
2021/4/15	2763	1053	2874	306	115	313	840	254	841	97	34	99	1539	435	1619	848	209	860	7137	35945	25528
2021/5/20	2713	1388	2928	270	124	287	775	196	749	82	27	84	1447	481	1540	792	255	835	7797	36811	26502
2021/7/5	3212	1811	3483	331	158	354	955	597	1069	113	45	114	1571	556	1691	877	181	902	8706	27297	22180
2021/9/24	3461	1816	3839	399	271	456	998	834	1275	119	49	119	1841	641	1892	989	387	1073	7397	40900	29570
2021/11/10	3395	1355	3629	339	154	351	975	368	1057	106	32	97	1758	460	1807	1018	315	1056	7723	23464	19976
2021/12/9	2765	1022	2773	261	113	279	796	266	813	80	25	79	1501	502	1580	851	221	871	7252	23548	18736
2022/1/27	2527	1596	2863	295	143	320	802	241	768	90	30	90	1524	524	1597	750	255	801	8357	24816	20659
2022/3/16	2753	1093	2906	263	114	277	779	224	778	83	26	82	1432	387	1543	860	231	868	7047	25115	19151
2022/5/11	2454	1223	2877	408	160	444	876	307	883	144	61	160	1605	578	1663	633	169	666	9420	3960	9914
2022/6/23	3394	2112	3867	703	445	828	1318	683	1448	300	88	277	2110	633	2174	541	362	610	5620	3460	6981
2022/9/16	4957	3813	6208	1277	1168	1764	1763	2744	2707	534	181	551	2635	973	2621	531	230	583	5055	3118	5981
Median	3040	1997	3465	351	507	483	941	969	1118	106	139	152	1649	697	1806	808	356	852	7168	27673	18676
Maximum	4957	3813	6208	1277	1168	1764	1763	2744	2707	534	181	551	2635	1087	2621	1133	682	1198	9420	40900	29570

Minimum	2321	988	2502	261	113	277	775	196	749	80	25	79	1432	387	1540	493	169	526	4610	2012	4922

Table 2 Calculate the monthly average drip rate.

Date	VIL-1B (Average Monthly drips/min)	VIL-10A (Average Monthly drips/min)	VIL-#3 (Average Monthly drips/min)
October-2019	8.71	2.41	0.09
November-2019	8.11	80.65	13.16
December-2019	28.52	120.85	18.41
January-2020	46.87	40.12	3.51
February-2020	51.69	62.73	9.28
March-2020	51.70	89.83	15.52
April-2020	39.66	12.44	3.59
May-2020	34.94	34.94	8.39
June-2020	25.37	9.31	2.81
July-2020	19.57	6.97	1.31
August-2020	14.58	5.02	0.56
September-2020	10.01	2.81	0.37
October-2020	7.61	2.90	0.50
November-2020	5.14	5.78	0.33
December-2020	4.61	57.31	9.05
January-2021	8.17	71.19	7.14
February-2021	49.19	108.15	19.78
March-2021	35.45	18.28	1.73

April-2021	28.22	10.58	1.42
May-2021	21.54	32.87	1.77
June-2021	28.23	17.67	0.70
July-2021	21.80	13.09	0.31
August-2021	17.91	9.13	0.82
September-2021	14.26	6.90	0.47
October-2021	10.31	4.94	
November-2021	8.77	3.63	Instrument stopped
December-2021	7.61	47.68	
January-2022	17.96	56.49	3.38
February-2022	28.37	41.11	5.32
March-2022	43.30	52.76	4.22
April-2022	44.05	51.24	5.03
May-2022	34.16	21.45	2.76
June-2022	23.17	7.81	1.77
July-2022	14.96	5.88	1.49
August-2022	11.71	5.21	1.04
September-2022	8.26		0.72
October-2022	4.02		0.46

Local meteorological rainfall and and temperature

Temperature correction for ERT calibration

Evapotranspiration

Infiltration flows : transfer processes, time delay

Water budget

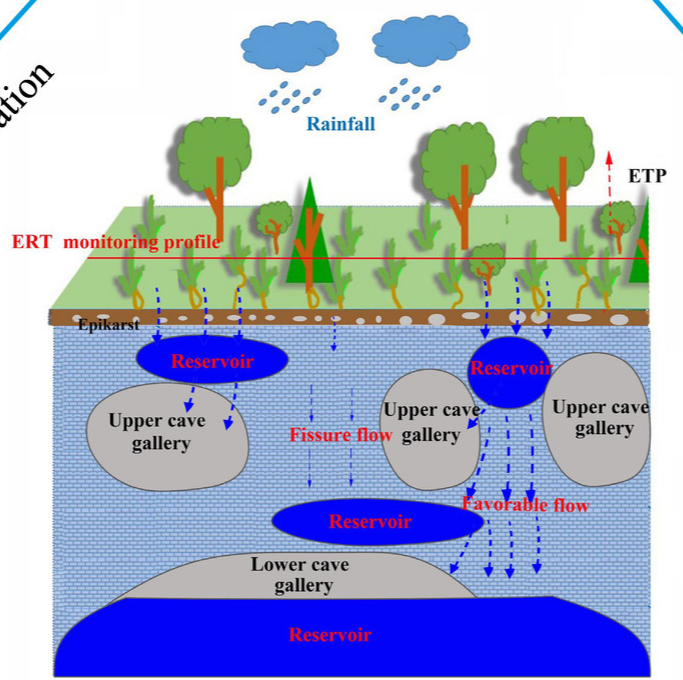

Electrical resistivity tomography

Cave drip water hydrology

(drip rate measurements under stalactites)

Karst reservoirs, infiltration pathways, seasonal changes